Reduced-Order Dynamics of a DC-Bus Voltage-Regulated Inverter for Steel Hardening Beyond Curie Point Temperature

Amaiur Mendi-Altube, Irma Villar, *Member, IEEE*, Claudio Carretero, *Senior Member, IEEE*, and Jesús Acero, *Senior Member, IEEE*

***Abstract*—We present a reduced-order dynamic model of an industrial induction heating system working beyond the Curie temperature and operated by a regulated input-voltage resonant inverter. On the one hand, a modular hardware design for power electronics is proposed, which allows great flexibility in operation while maintaining simplicity in its control. On the other hand, a co-simulation model has been derived to ensure inverter control stability under the variable operating conditions intrinsically associated with the physical properties of the induction load. This model is based on applying a reduction of the parameters obtained from simulations carried out by employing a finite element analysis tool to use the results in CAE simulation software. To validate the obtained experimental results, a comparison has been made with the numerical results obtained from the simulation.**

***Index Terms*—induction heating, inverter, nonlinear load, dynamic modeling, Curie temperature, finite elements.**

I. Introduction

INDUCTION HEATING (IH) technique has gained significant attention in recent years due to its potential to replace traditional heating technologies in various fields, e.g., industrial, household, or medical applications [1], [2]. Induction heating is a contactless, efficient, easy-to-control, fast, and durable heating system that offers numerous advantages over other traditional heating technologies [3].

The general power conversion scheme for IH systems is shown in Fig. 1. The main feature of this type of system is the IH load, composed of a coil and the workpiece, whose electrical equivalent consists of an inductance, L, in series with a resistance, R, [4]. The ac-dc rectifier supplies the dc-bus from the ac mains voltage. The simplest constructions consist of diode bridge rectifiers, although controlled options have advantages [5], [6]. On the other hand, the dc-ac stage

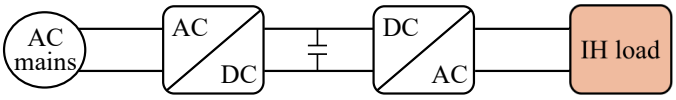

Fig. 1. Basic structure of an IH system.

generates the medium frequency current that will feed the inductive type load. The different configurations used distinguish between the type of electronics employed, either single switch [7], [8], half-bridge [9] or full-bridge topologies [10]. Depending on the structure of the resonant tank, a distinction can be made between LC-series [11], [12], which stands out for its simplicity; LC-parallel [13], [14], that achieves favorable working conditions for the electronic inverter but increasing the control complexity; and LCL [15], [16], which features robustness. Recently, proposals have also been made for direct ac-ac converters applied to induction heating, but the larger number of devices to be switched complicates the generation of gating signals [17]–[19]. Additionally, there are several proposals for multiple output topologies [20], [21], mainly focused on specific applications.

Different modulations can be applied to vary the power delivered to the inductor-workpiece system. Taking advantage of the resonance curve of the IH systems, Frequency Density Modulation, FDM, [22], [23] is usually applied. On the other hand, in the case of using full-bridge inverters, it is possible to apply Phase-Shift Modulation, PSM, [24]. Finally, Pulse Density Modulation, PDM, [25], [26] stands out due to its simplicity. Several methods for resonant inverters in IH systems have been proposed regarding control variables. The control of the induction coil current is discussed in [27]; strategies focused on temperature control are proposed in [28]; and power regulation is addressed in [29], [30]. The dynamic behavior of the inductor-workpiece load has been described in some works, although it is not fully captured due to the complex dependencies of the physical properties of the inductor [31].

The electrical behavior of the inductor-workpiece system depends on electromagnetic, thermal, and metallurgical factors. Electromagnetic-thermal numerical simulations are needed to fully describe this behavior [32]–[35]. On the other hand, some works have been devoted to study the dynamics of power converters applied for IH heating. An analysis based on experimental results is proposed in [36]. The robustness

Manuscript received October 3, 2024.

Amaiur Mendi-Altube is with the Department of Energy Storage and Power Electronics, Ikerlan Technology Research Centre, Basque Research and Technology Alliance (BRTA), 20500 Arrasate-Mondragón, Spain, and also with the Department of Electronic Engineering and Communications, Universidad de Zaragoza, 50018 Zaragoza, Spain (e-mail: amendi@ikerlan.es/867467@unizar.es).

Irma Villar is with the Department of Energy Storage and Power Electronics, Ikerlan Technology Research Centre, Basque Research and Technology Alliance (BRTA), 20500 Arrasate-Mondragón, Spain (ivillar@ikerlan.es).

Claudio Carretero is with the Department of Applied Physics, Universidad de Zaragoza, 50009 Zaragoza, Spain (e-mail: ccar@unizar.es).

Jesús Acero is with the Department of Electronic Engineering and Communications, Universidad de Zaragoza, 50018 Zaragoza, Spain (e-mail: jacero@unizar.es).

of the control of an induction hardening system can be found in [37]. In [38] the dynamics of the induction load is studied by applying phase shift control and in [39] an analysis of the dynamics of a matrix power converter is performed but both focused exclusively on the circuit behavior of the IH load, which need to be properly identified. However, the co-simulation of the power electronics and the induction load, including its complex dependencies between the temperature and the magnetic and resistive properties, is still challenging and computationally expensive. Therefore, a reduced-order model that can diminish the computational burden without significantly sacrificing accuracy is highly recommended.

This paper is an extension of the work entitled "Dynamic DC-Bus Voltage Control of Induction Hardening System Under Load Temperatures from Ambient to Beyond Curie Point", [40], presented on the IEEE Applied Power Electronics Conference and Exposition (APEC) 2024 in Long Beach, CA. This extended paper not only focuses on the dynamic dc-bus voltage control at fixed switching frequency of the IH process, but it goes into more detail regarding the electromagnetic-thermal modeling by Finite Element Method (FEM) of the inductive load, considering the material's nonlinear electric, magnetic, and thermal properties, and their inter-dependencies.

The remainder of this paper is organized as follows. Section II describes the versatile power converter used for both modeling and simulation. Section III provides the characteristics of the electromagnetic-thermal model of the nonlinear induction load implemented in a finite element analysis tool. Section IV gives the procedure to reduce the results of the above model for using in a circuit simulation tool. Experimental validation of the results is given in Section V. Finally, some conclusions are drawn in Section VI.

II. DC-Bus Voltage-Regulated Inverter for Flexible Feeding of Light Inductive Load

A. Proposed Electronic Topology

The induction heating system required for industrial hardening must work under a wide range of conditions to achieve accurate thermal processing of materials. This system involves a nonlinear, light, inductive load, where the equivalent impedance depends on both the workpiece's temperature distribution and the applied excitation level during processing.

In order to facilitate the control of the power converter, a versatile inverter topology able to supply the required power to loads of varying characteristics while maintaining robust behavior is proposed. The power converter has to be able to control the power delivered to the load despite the change in its properties with the purpose of modulating the metallurgical process in the workpiece. Moreover, it should cover a wide range of power levels to ensure proper operation. Additionally, the electronics has to be capable of handling inductive loads with a small resistive component, which may vary considerably throughout the hardening. The basic structure of the proposed system is illustrated in Fig. 2.

This proposal was designed to prioritize both flexibility and robustness, under a wide variety of operational requirements. That is the main reason why the intermediate dc-dc stage was added. The current modular design not only improves functionality but also provides a clear pathway for upgrades and adjustments, making it a practical choice for a wide range of applications.

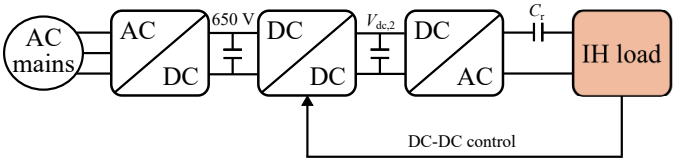

Fig. 2. Schematic of the proposed IH system for hardening of metallic workpieces.

The induction heating system operates by supplying a medium-frequency current to the load. The heating element consists of a solenoidal type coil with few turns. When operating without a workload, the system load is mainly inductive with a small resistive component due to losses in the wiring and winding. When the workpiece is inserted, the equivalent inductance of the system may change according to the temperature and magnetic conditions, and the system resistance increases due to power delivery to the load. Induction heating generates high heat flux to the workpiece's surface, and therefore, controlling the delivered power enables the precise application of metallurgical treatment to the workpiece's superficial layer.

In this proposal, the power electronics is designed using three sequential stages, as shown in Fig. 3, to achieve a versatile operation. Firstly, a three-phase rectifier featuring controlled switching devices transforms mains voltage into a low-ripple dc-bus. Secondly, a dc-dc buck converter regulates the dc-bus voltage level to feed the last electronics stage. The output voltage of this stage becomes the variable to be controlled for regulating the power delivered to the workpiece. The dynamics of the dc-bus voltage are determined by the evolution of the impedance associated with the workpiece throughout the metallurgical treatment cycle. Finally, the third power stage consists of an inverter operating at a fixed switching frequency, determining the power delivered from the input voltage provided by the dc-bus. The physical implementation of the complete electronic stage is captured in Fig. 4.

B. Practical Implementation

The first electronic stage includes a three-phase boost-type controlled rectifier that converts the 380 V, 50 Hz three-phase mains voltage into a 650 V dc-bus voltage. A vector control integrating a power factor corrector has also been included to ensure a low ripple output and power factor close to one at the input by canceling the reactive power consumption. In addition, in order to comply with existing standards, a Schurter FMBC-A91G-J010 EMC filter and an LCL filter were placed at the input of the converter. The controlled devices used are three Wolfspeed CAB425M12XM3 1200 V and 425 A SiC modules, each implementing a half-bridge inverter composed of two MOSFETs with $R_{\mathrm{ds}} = 3.5$ mΩ. A Dual channel differential isolated gate driver XM3 CPM3 SiC connected to each module has been used to generate the trigger signals

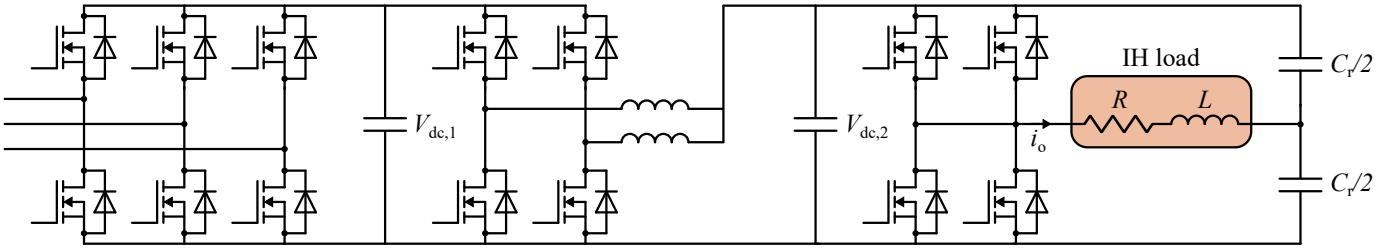

Fig. 3. Power electronics converter for the IH industrial applications test bench: 3-phase rectifier, dc-dc buck, and half-bridge inverter with inductive load and resonant capacitors.

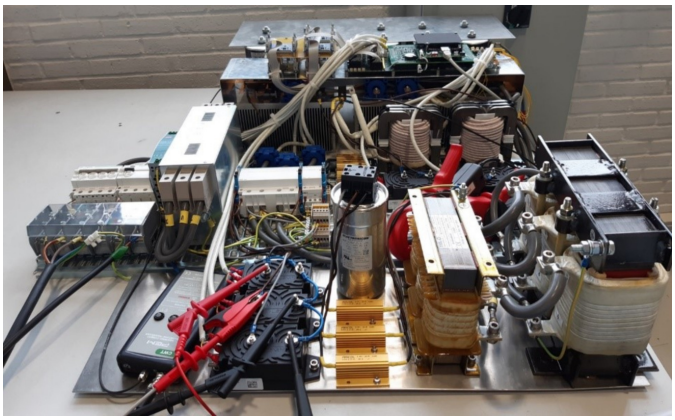

Fig. 4. Power electronic converter.

at a fixed switching frequency of $f_{3-\mathrm{ph}} = 16.67$ kHz. The control of the modules is achieved by applying asymmetrical voltage control by modifying the duty of each module. The output of the controlled three-phase rectifier consists of a bus capacitor $C_{\mathrm{dc},1} = 600$ μF in a configuration of six KEMET C44UOGT6100A8TK 100 μF capacitors connected in parallel to provide a low ripple 650 V bus voltage.

The intermediate power stage consists of a dc-dc buck converter regulating the variable bus voltage $V_{\mathrm{dc},2}$. In this case, two inverting branches working in two-channel interleaved mode is used, each consisting of a Wolfspeed CAB425M12XM3 SiC module. Fixed switching frequency modulation at $f_{\mathrm{buck}} = 16.67$ kHz is used, applying asymmetrical voltage control on each branch. At the output of each of the inverting branches, a 330 μH inductor has been placed, and the regulated bus voltage, $V_{\mathrm{dc},2}$, is obtained by means of the filtering provided by the bus capacitor $C_{\mathrm{dc},2} = 400$ μF in a configuration of four KEMET C44UOGT6100A8TK capacitors of 100 μF connected in parallel. The regulated bus voltage, $V_{\mathrm{dc},2}$, dynamics will be determined by the power cycle to be delivered in the hardening process.

Finally, the output stage will comprise two half-bridge inverters working in parallel at a fixed switching frequency of $f_{\mathrm{sw}} = 14.2$ kHz. Two Wolfspeed CAB425M12XM3 SiC modules have been used, and a series LC-circuit has been selected as the resonant tank to optimize the delivered power. The value of the resonant capacitor is 36.4 uF. Working at a fixed switching frequency makes the work of the ac-dc converter independent of the output power regulation, simplifying the control of the electronics.

C. Digital Control

The entire system was controlled using a digital system implemented in a National Instruments sbRio 9607 embedded controller. The trigger signals for the 3-phase rectifier were generated from the measurements of the current and voltage signals of each phase and the output voltage $V_{\mathrm{dc},1}$. We used a 200 A rms LEM LF 210-S current transformer for the current measurements and a LEM DVL 250 voltage transducer for the voltage measurements of each phase of the mains, respectively. The voltage at the output of the 3-phase rectifier was monitored with a LEM DVL 750-UI voltage transducer.

To generate the regulated dc-bus, $V_{\mathrm{dc},2}$, through the dc-dc buck, the current delivered to the load, i_{o}, was used as the control variable. The current setpoint, I^*_{rms}, was provided through a CAN-bus communication in an open loop system, allowing flexibility in the cycle to be applied depending on the type of workpiece under treatment. Additionally, the current supplied by each branch of the dc-dc buck stage, monitored by two 200 A rms LEM LF 210-S current transformers, was also used as input. The bus voltage $V_{\mathrm{dc},2}$ was provided by a LEM DVL 750-UI voltage transducer. The current delivered to the load was determined by measuring the current of each of the two half-bridges working in parallel using a 300 A rms LEM LF 306-S Hall current probe. The trigger signals were generated by two PWMs of the same frequency as the 3-phase rectifier, $f_{\mathrm{buck}} = 16.67$ kHz, and out of phase by 180º to reduce the interference generated by the system when applying interleaving of the two branches.

Finally, the gating signals of the two half-bridges are generated as fixed frequency signals $f_{\mathrm{sw}} = 14.2$ kHz, which is high enough to ensure the ZVS conditions at the interest heating treatments despite the existing small inductance variations.

The specific definition of the power cycle to be applied will be obtained empirically in the future for each of the workpieces to be treated, ensuring the repeatability of the process. The proposed control includes overcurrent protection so that the modulation in the half-bridge inverter is suppressed when a malfunction is detected.

III. Electromagnetic-Thermal Model of Non-Linear Induction Load

A. Characteristics of Induction Load

The system load is mainly inductive with some resistive contribution, resulting in a primarily reactive equivalent

impedance. The workpiece processing requires the system to operate under varying conditions due to the load fluctuations over time. This complexity requires simple and robust system designs. When the system operates without the workpiece inside the coil, the load exhibits a stable equivalent inductance under different working conditions, such as switching frequency, current level, or temperature variations. In any case, there is a resistive component associated with current losses through the coil, the connecting cables, the ESR of the resonance capacitors, and, to a lesser extent, the resistance of the printed circuit board tracks. When the metal workpiece is inserted, the load inductance is altered due to two opposing phenomena: induced currents on the surface tend to reduce the magnetic energy stored by the coil, while the magnetic properties of the load tend to increase it. Nonetheless, the inductance variation, although noticeable, only represents a fraction of the total inductance, owing to the coil's construction and the workpiece's dimensions. Additionally, a resistive component is involved in transferring energy to the workpiece, attributed to the dissipation of the currents induced by the variable magnetic field on the material's surface.

The characteristics of the load determine the selection of the inverter resonant tank. A series resonant tank has been chosen by connecting the corresponding resonance capacitor because it allows simple control of the current flowing through the load, facilitating the real-time regulation of the power delivered to the load under time-varying conditions. Alternative resonant tank topologies have been used in induction heating systems, including the LCL resonant tank, which allows reducing the current delivered by the electronic stage but whose controllability is more complex. As the inverter stage will work at a fixed switching frequency, a resonance capacitor has been chosen to ensure that the resonance frequency is always below the working frequency, thus guaranteeing smooth switching conditions, while there is no excessive difference between the two frequencies, which would impede the delivery of the required power.

The distribution of electromagnetic fields in the workpiece is determined by the current flowing through the winding. Since the material has ferromagnetic properties, its response to electromagnetic fields is characterized by the B-H curve. The maximum field level reached in each switching cycle plays a crucial role. Therefore, it is appropriate to consider the dependence on the current envelope associated with the maximum reached in each switching cycle. The current envelope varies smoothly, which can be associated with a moderate equivalent impedance variation. Another important consideration is that the temperature of the part has a variation in relation to its main axis. Selecting the temperature of the intermediate region of the workpiece as the reference temperature seems convenient, as it is the region with higher field values and power density transfer; moreover, after comparing temperatures at different coordinates of the billet, it has been concluded that it is when this point saturates that the equivalent resistance and inductance change their behavior drastically. However, it is important to keep in mind that the effect of temperature distribution irregularities can significantly influence the heating treatment, particularly in processes that are slower. It's essential to establish the dynamics of the converter to ensure safe working conditions, as the working conditions change throughout the power cycle.

B. Computational Model of the Nonlinear Induction Load

Induction heating involves the combination of electromagnetism, heat transfer, and metallurgy. For this reason, numerical simulation tools that incorporate multiphysics analysis are necessary to obtain the equivalent impedance of the inductor-workpiece system. The changes in the metallurgical structure of the workpiece will not be discussed in detail, as they are accounted for in the variation of the material's physical properties with temperature. Therefore, it will be necessary to create an electromagnetic-thermal model that considers the nonlinear properties of the induction load to accurately estimate the equivalent impedance.

Regarding the electromagnetic modeling of the inductor-workpiece system, it will be based on the following assumptions: first, only the response at the operating frequency will be considered, as this is the fixed working frequency of the inverter, and the current in the coil corresponds mainly to the fundamental harmonic. Second, the model will just consider the inductive effects of the current flowing through the coil. This means that the source of the electromagnetic fields is associated with the uniform current distribution, denoted as $\mathbf{J}_{\text{coil}}$ in the turns section of the winding. Consequently, the magnetic potential vector, $\mathbf{A}$, will describe the system's fields. The electric field is given by $\mathbf{E} = -\partial_t \mathbf{A}$ and the magnetic field is given by $\mathbf{B} = \nabla \times \mathbf{A}$.

The fields are obtained by solving the diffusion equation for the magnetic vector potential [41]:

$$\sigma \partial_t \mathbf{A} - \frac{1}{\mu} \nabla^2 \mathbf{A} = \mathbf{J}_{\text{coil}} \tag{1}$$

where σ is the conductivity and μ is the permeability of the material media.

The primary challenge lies in accurately representing the nonlinear properties of the workpiece, which are dependent on the field levels at each point and the temperature distribution. In eddy current problems, obtaining results in the frequency domain is generally more straightforward. In this domain, the equation simplifies to $j\omega\sigma\mathbf{A} - \frac{1}{\mu}\nabla^2\mathbf{A} = \mathbf{J}_{\text{coil}}$, where the angular frequency $\omega = 2\pi f$.

To address the diffusion equation (1), a crucial step involves discretizing the system's geometry using a mesh. In general, the mesh elements used in numerical simulations should be smaller than the characteristic distances over which the modeled fields vary. In the case of electromagnetic simulations involving induction loads, there is a rapid exponential variation when the fields enter a conductive material, which is determined by a characteristic distance known as the penetration depth, δ, [42]. Therefore, it is essential to include several mesh elements that are a fraction of the penetration depth when modeling the induction charge. This requirement leads to a high number of degrees of freedom that need to be solved, resulting in increased computational costs. To address the challenges of meshing the induction charge, the impedance

boundary condition (IBC) is applied. By using this IBC, it is possible to achieve accurate simulation results while significantly reducing computational costs. Thus, given that the characteristic dimensions of the system are on the order of millimeters, it can be confirmed that the results derived from applying the IBC are accurate, [43].

However, when working with nonlinear material properties and the saturation of the billet by the magnetic field, the treatment becomes notably complicated. To face this challenge, an equivalent magnetic permeability, μ, dependent on the magnetic field amplitude and material temperature, is derived via 1-D numerical simulation, as detailed in [44]. This procedure has also been described for a practical COMSOL simulation in the paper [45]. Combining this equivalent permeability with the boundary impedance condition yields accurate electromagnetic modeling without excessive computational costs. As a result, the power distribution on the workpiece surface and the equivalent electrical impedance of the inductor-workpiece system are obtained, the latter being:

$$Z = \frac{V_{\mathrm{ind}}}{I_{\mathrm{coil}}} = -\frac{1}{I_{\mathrm{coil}}}\frac{1}{S_{\mathrm{turn}}}\int_{v_{\mathrm{coil}}} E_{\parallel} dv \tag{2}$$

where V_{ind} is the voltage induced in the winding, I_{coil} is the current amplitude flowing through the winding, S_{turn} is the cross-sectional area of a turn, v_{coil} the volume of the coil, and $E_{\parallel}$ is the electric field longitudinal to the turns of the coil.

Concerning the thermal behavior of the workpiece, it is essentially determined by the expression of heat diffusion in the workpiece because the delivered powers are high and metals are good thermal conductors:

$$\rho c_{\mathrm{p}} \partial_t T - \nabla(k \nabla T) = Q \tag{3}$$

where ρ is the density of the material, c_{p} is the specific heat, k is the thermal conductivity, and Q is the heat source arising from eddy currents, $Q = \frac{1}{2\sigma}|\mathbf{J}_{\mathrm{coil}}|^2 = \frac{\sigma\omega^2}{2}|\mathbf{A}|^2$.

Heat capacity values play a crucial role in temperature evolution since they represent the amount of energy required to raise the temperature at each point, as well as the energy needed to increase the temperature of the entire workpiece. In conclusion, accurately modeling the transient behavior of temperature requires considering both thermal conductivity and heat capacity, as they are essential factors.

The thermal processes encompass thermal radiation, which holds significant importance at elevated temperatures, and thermal convection, whose impact becomes notable when the part is subjected to quenching through a water shower.

Unlike its electromagnetic counterpart, the thermal model will be executed in the time domain. Consequently, when substantial variations in physical properties occur due to changes in temperature distribution, a new electromagnetic simulation in the frequency domain will be performed.

C. Computational Simulation Results of the Inductor-Workpiece System

In industrial induction heating processes, solenoid-shaped windings are commonly used with cylindrical workpieces. In this article, the inductor-workpiece system has the geometrical dimensions shown in Table I. The current flows through a solenoid-shaped coil consisting of 6 turns of radius 18 mm, spaced 9 mm apart. Copper tubing has been used in its construction to allow liquid cooling by circulating water so that at all times, its operating temperature is guaranteed to be below the boiling point of water. The copper tube has an outer diameter of 6 mm and an inner diameter of 4 mm. The metal part to be heated consists of a 42CrMo4 - AISI 4140 steel cylinder of radius 10 mm and length 75 mm.

TABLE I
IH LOAD'S GEOMETRY

Parameter	Value	Unit
Coil's turn number	6	
Coil's inner radius	15	mm
Turn inner diameter	4	mm
Turn outer diameter	6	mm
Distance between turns	9	mm
Billet radius	10	mm
Billet length	75	mm

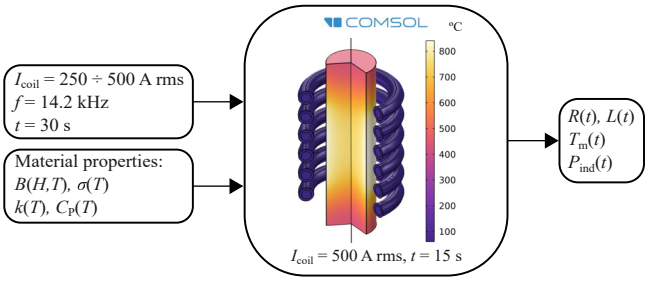

Fig. 5. Schematic of the electromagnetic-thermal Comsol-based simulation.

The 42CrMo4 steel has been thoroughly employed in literature because it is a typical steel used in industrial hardening applications through electromagnetic induction. It is a well-known material, and its properties are known. Therefore, these properties can be directly implemented in electromagnetic-thermal simulations, reducing the computational and economic costs of the characterizing process. The physical properties of this common steel are compiled in [46]. Although the temperature of the material considerably influences all the physical properties of importance, the disappearance of the magnetic properties from the Curie temperature, $T_{\mathrm{C}} = 783$ ºC, which is reflected, in turn, in a substantial variation of the thermal capacity of the material, stands out especially. From the analytical expression of the B-H curve with respect to temperature presented in [47], it is straightforward to apply the methodology proposed in [44] to obtain the equivalent magnetic permeability of the material with respect to field and temperature.

In order to obtain simulation results, a commercial finite element-based analysis tool, which integrates electromagnetic simulation with thermal simulation, such as Comsol Multiphysics®, has been used, as schematically depicted in Fig. 5. Transient simulations of 30 s duration have been performed, starting with the part at room temperature. In each simulation, a current of 14.2 kHz and fixed amplitude ranging from 250 A rms to 500 A rms has been applied, covering a wide range of operating conditions.

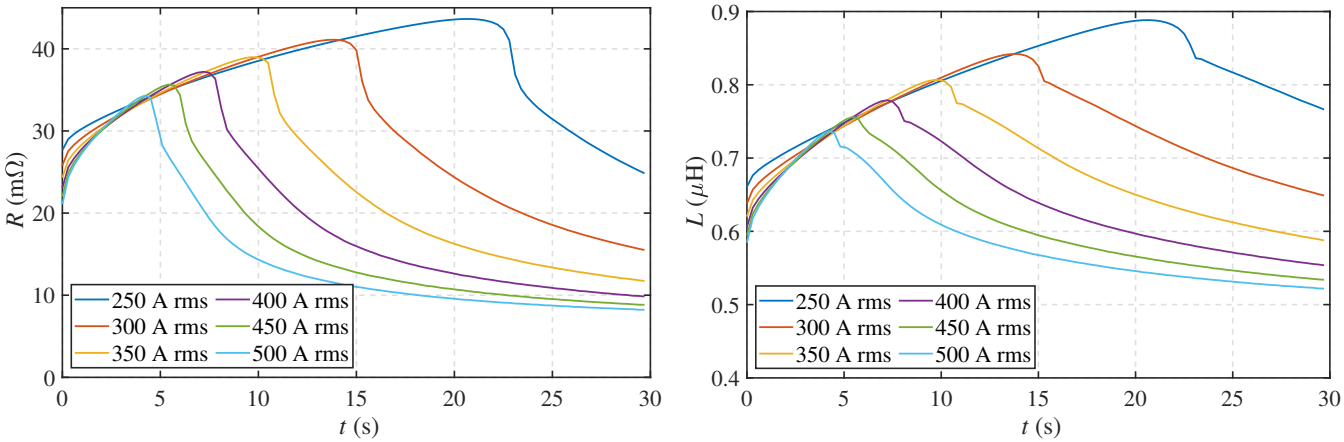

Fig. 6. Simulation results for a transient of 30 s: (a) equivalent resistance, R, (b) equivalent inductance, L.

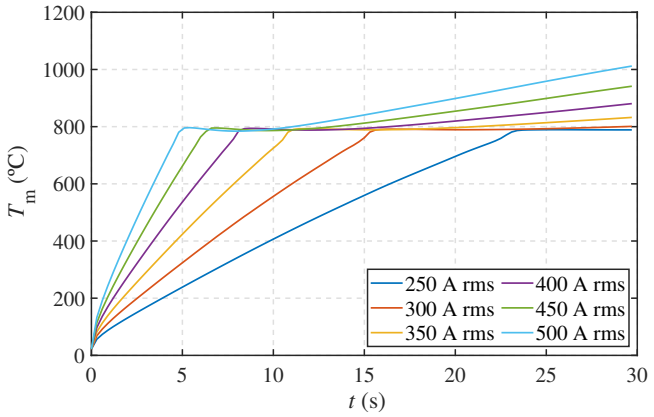

Fig. 7. Temperature in the middle region of the billet's surface, T_{m}.

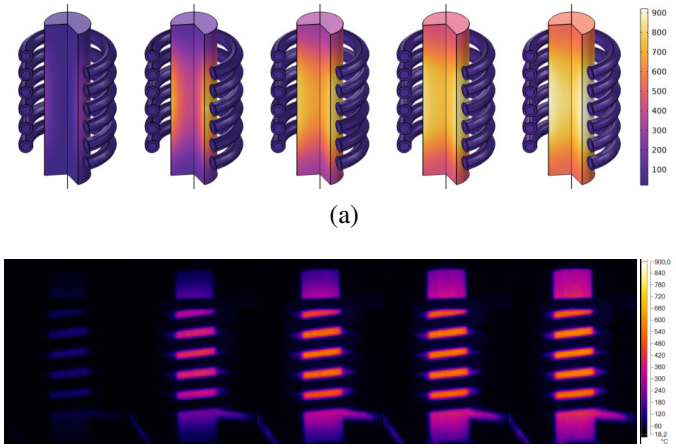

Fig. 8. Temperature distribution through the billet with 500 A rms and 14.2 kHz coil's current at t = 1, 5, 10, 15, and 20 s, respectively: (a) Comsol-based thermal simulation, and (b) thermal camera captures during the experimental heating process.

In Fig. 6, the results of the equivalent impedance of the inductor-workpiece system, $Z = R + j\omega L$, are plotted. In Fig. 6a, it can be seen how the equivalent resistance initially increases due to the temperature increase of the workpiece, but its value starts to decrease, possibly due to the magnetic saturation of a region of the workpiece exceeding the Curie temperature. The volume of this saturated region increases with time. On the other hand, in Fig. 6b, a similar behavior of the equivalent inductance, L, is observed, although with a smaller relative variation.

The temperature distribution of the workpiece shows high gradients due to the high transferred power levels. In Fig. 7, the temperature of the central region of the workpiece, T_{m}, has been plotted to observe its behavior as it approaches close to the Curie point of the material. It is observed that T_{m} stops increasing abruptly because the efficiency of the induction energy transfer process decreases as the magnetic properties are lost.

D. Comparison of Electromagnetic-Thermal Simulations and Experimental Measurements

In this section, the finite-element thermal simulations are compared with an experiment realized on the induction hardening test bench in Fig. 8. The heating process was recorded with a Fluke RSE300 thermal camera to compare the simulated and real temperature distributions during the heating process. Both the simulation and test are carried out under 500 A rms and 14.2 kHz coil's current excitation. With these working conditions, the steel billet should be heated for 30 seconds to reach the desired temperature in the central areas of the billet's surface.

The temperature distribution on the surface of the workpiece, as illustrated in both Fig. 8a and Fig. 8b, is notably inhomogeneous. However, it exhibits a clear pattern where the maximum temperature is found in the central zone of the billet. Temperatures significantly above the Curie temperature are not observed, primarily due to magnetic saturation and,

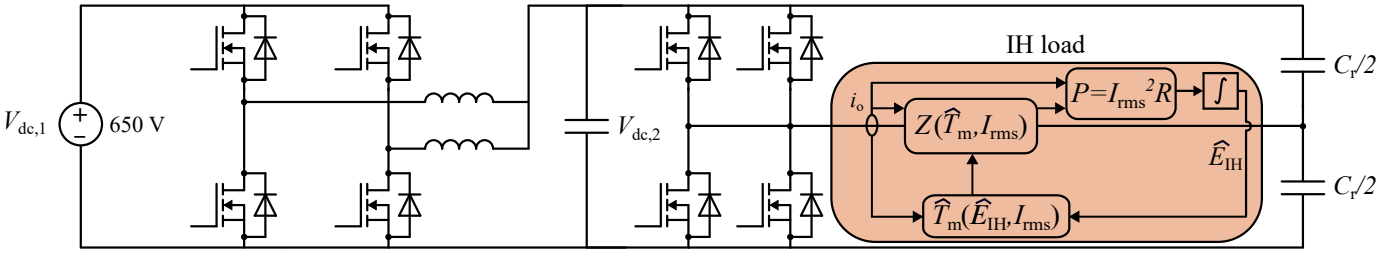

Fig. 9. Schematic of the dynamic model: dc-dc buck, inverter, and reduced-order IH load.

to a lesser extent, the increased heat capacity. In the capture of images with the thermal camera, a behavior that performs as a gray body of the workpiece is assumed, with properties that remain consistent throughout the process. This means that the emissivity is considered independent of the wavelength and remains constant with respect to the temperature. As shown in Fig. 8, there is a considerable correlation between the simulation and experimental results, indicating that the electromagnetic-thermal simulation has been validated.

IV. Reduced-Order Dynamic Model

A. Inductor-Workpiece Equivalent Impedance

The results from the previous Section provide a good description but are not practical for predicting the entire system's performance because of the high computational cost. It can be beneficial to combine the simulation results from the finite element analysis tool with electronic circuit simulation software like Matlab/Simulink®. An accurate definition of the reduced-order model based on physical considerations for modeling the induction-workpiece load and its inclusion into the electronic simulation tool can be valuable.

The equivalent impedance of the induction load with the workpiece has several parameter dependencies. Although it does not constitute a complete description of the electrical behavior, it is appropriate to indicate that the equivalent impedance can be determined as follows since it presents a good balance between complexity and descriptive power:

$$Z\left(f, I_{\mathrm{rms}}, \hat{T}_{\mathrm{m}}\right) = R\left(f, I_{\mathrm{rms}}, \hat{T}_{\mathrm{m}}\right) + j\omega L\left(f, I_{\mathrm{rms}}, \hat{T}_{\mathrm{m}}\right), \tag{4}$$

where f represents the working frequency, and I_{rms} is related to the amplitude of the applied current, and $\hat{T}_{\mathrm{m}}$ is the estimated temperature of the central region of the workpiece.

The proposed reduced-order equivalent impedance at a fixed frequency will be represented as $Z\left(I_{\mathrm{rms}}, \hat{T}_{\mathrm{m}}\right) = R\left(I_{\mathrm{rms}}, \hat{T}_{\mathrm{m}}\right) + j\omega L\left(I_{\mathrm{rms}}, \hat{T}_{\mathrm{m}}\right)$, which is represented inside the highlighted area in Fig. 9. The detailed procedure to estimate the equivalent impedance of the IH-load $Z\left(I_{\mathrm{rms}}, \hat{T}_{\mathrm{m}}\right)$ will be detailed as follows.

B. Current Level and Estimated Temperature

In the reduced-order model, the level of current feeding the inductor-workpiece system plays an important role. As mentioned in assumptions, the current has almost the only component at the fundamental frequency. Therefore, being a practically sinusoidal waveform, the relationship between the current amplitude and its root mean square value, I_{rms}, is immediate, so both values can be used interchangeably. Note that the current I_{rms} will be determined by the operational conditions in the circuit simulation model.

On the other hand, the reduced-order model also depends on the temperature, T_{m}, in the central region of the workpiece; and at the same time, T_{m} depends on the total energy delivered to the workpiece, $\hat{E}_{\mathrm{IH}}$, obtained from the integral of the delivered power at each moment. Moreover, a second factor related to the heating rate of the workpiece is also considered in the T_{m} estimation. The heating rate will be given by the amplitude of the current, I_{rms}, with which the load is fed. In order to simplify the treatment, a factorization into two terms, each dependent on the estimation of the total energy, $\hat{E}_{\mathrm{IH}}$, and the current, I_{rms}, respectively, is proposed as follows:

$$\hat{T}_{\mathrm{m}}(\hat{E}_{\mathrm{IH}}, I_{\mathrm{rms}}) = \hat{T}_{\mathrm{E}}(\hat{E}_{\mathrm{IH}}) \cdot \hat{T}_{\mathrm{I}}(I_{\mathrm{rms}}) \tag{5}$$

where $\hat{T}_{\mathrm{E}}(\hat{E}_{\mathrm{IH}})$ and $\hat{T}_{\mathrm{I}}(I_{\mathrm{rms}})$ are factors dependent on the provided energy to the workpiece and the current level, respectively.

The temperature of the workpiece has different dependencies according to the regions observed in Fig. 7; this approach considers two dependencies. The induction energy transfer process is more efficient below the Curie temperature, T_{C}, where the material possesses ferromagnetic properties. Above T_{C}, a phase transition occurs where the material no longer has magnetic properties and the temperature rise is slower. In order to capture this behavior, the following temperature factors are proposed with respect to the estimated delivered energy:

$$\hat{T}_{\mathrm{E}}(\hat{E}_{\mathrm{IH}}) = \begin{cases} T_0 + C_{\mathrm{T_E}} \hat{E}_{\mathrm{IH}}^{n_{\mathrm{T_E}}} & \hat{T}_{\mathrm{m}} < T_{\mathrm{C}} \\ T_{\mathrm{brk}} + C'_{\mathrm{T_E}} (\hat{E}_{\mathrm{IH}} - E_{\mathrm{brk}})^2 & \hat{T}_{\mathrm{m}} \geq T_{\mathrm{C}} \end{cases} \tag{6}$$

where $T_0 = 22$ ºC is the initial temperature, $n_{\mathrm{T_E}} = 0.6777$ and $C_{\mathrm{T_E}} = 0.6055$ are the exponent and proportionality factor, respectively, fitted to a potential function for the dependence below the Curie temperature. E_{brk} and $C'_{\mathrm{T_E}} = 4.0017 \times 10^{-8}$ are the cumulative energy to reach the Curie temperature in the above temperature range and the factor of proportionality of the quadratic dependence with excess energy from the Curie temperature, respectively.

Regarding the current-dependent factor $\hat{T}_{\mathrm{I}}(I_{\mathrm{rms}})$, a simpler expression has been considered because of its minor

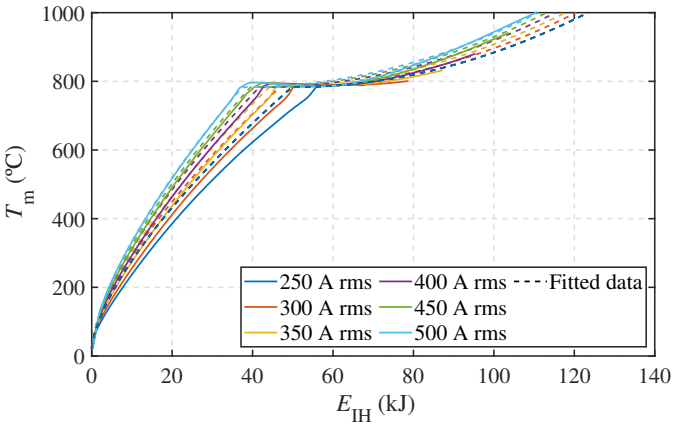

Fig. 10. Comparison of simulated data and fitted curves for the middle point temperature of the billet's surface.

importance, including only the dependence below the Curie temperature, as follows:

$$\hat{T}_{\mathrm{I}}(I_{\mathrm{rms}}) = \begin{cases} \frac{\sum_{\mathrm{i}=0}^{2} C_{\mathrm{T_I,i}} I^{i}}{\sum_{\mathrm{i}=0}^{2} C_{\mathrm{T_I,i}} I_{\mathrm{ref}}^{i}} & \hat{T}_{\mathrm{m}} < T_{\mathrm{C}} \\ 1 & \hat{T}_{\mathrm{m}} \geq T_{\mathrm{C}} \end{cases} \tag{7}$$

where the adjustment provides the coefficients $C_{\mathrm{TI},0} = 621.1191$, $C_{\mathrm{TI},1} = 0.6627$, and $C_{\mathrm{TI},2} = 1.0691 \times 10^{-5}$, respectively.

In Fig. 10, the comparison between fitted curves and simulation results in Comsol® with respect to the temperature in the central region of the workpiece is shown. As can be seen, the fit is quite good, although a larger error is observed at the lowest values of current, I_{rms}, due to the difficulty of capturing the behavior accurately with a small number of parameters. In any case, the accuracy achieved will be sufficient to obtain valid results.

C. Impedance Dependence on the Estimated Parameters

Polynomial expressions are used to model the equivalent impedance $Z\left(I_{\mathrm{rms}}, \hat{T}_{\mathrm{m}}\right)$ because they provide an analytical solution that can precisely capture an extended range of behaviors. The equivalent resistance (R) and inductance (L) expressions are dependent on the estimated temperature, $\hat{T}_{\mathrm{m}}$, and current level, I_{rms}. These expressions are obtained by factorizing each dependency equation, as it is provided as follows:

$$R(I_{\mathrm{rms}}, \hat{T}_{\mathrm{m}}) = R_{\mathrm{T}}(\hat{T}_{\mathrm{m}}) \cdot R_{\mathrm{I}}(I_{\mathrm{rms}}) \tag{8}$$

and

$$L(I_{\mathrm{rms}}, \hat{T}_{\mathrm{m}}) = L_{\mathrm{T}}(\hat{T}_{\mathrm{m}}) \cdot L_{\mathrm{I}}(I_{\mathrm{rms}}) \tag{9}$$

The expressions for (8) and (9) have a similar structure but with different coefficients. These coefficients are associated with the temperature, $\hat{T}_{\mathrm{m}}$, and current level, I_{rms} dependencies, respectively. The fitting is divided in the two regions delimited by the material's Curie Temperature, T_{C}: below and above the Curie temperature, T_{C}, with a transitional temperature ΔT to ensure stability in the simulation without sacrificing precision. Additionally, the temperature dependence requires a higher order polynomial compared to the current dependence to accurately approximate the behavior.

The factors for the temperature dependence are as follows:

$$R_{\mathrm{T}}(\hat{T}_{\mathrm{m}}) = \begin{cases} \sum_{\mathrm{i}=0}^{6} C_{\mathrm{R_T,i}} \hat{T}_{\mathrm{m}}^{i} & \hat{T}_{\mathrm{m}} < T_{\mathrm{C}} \\ \sum_{\mathrm{i}=0}^{3} C'_{\mathrm{R_T,i}} \hat{T}_{\mathrm{m}}^{i} & \hat{T}_{\mathrm{m}} \geq T_{\mathrm{C}} + \Delta T \end{cases} \tag{10}$$

and

$$L_{\mathrm{T}}(\hat{T}_{\mathrm{m}}) = \begin{cases} \sum_{\mathrm{i}=0}^{6} C_{\mathrm{L_T,i}} \hat{T}_{\mathrm{m}}^{i} & \hat{T}_{\mathrm{m}} < T_{\mathrm{C}} \\ \sum_{\mathrm{i}=0}^{3} C'_{\mathrm{L_T,i}} \hat{T}_{\mathrm{m}}^{i} & \hat{T}_{\mathrm{m}} \geq T_{\mathrm{C}} + \Delta T \end{cases} \tag{11}$$

Conversely, no current level dependence, I_{rms}, is observed above the Curie temperature, T_{C} as the magnetic properties of the workload vanish, and consequently, the equivalent impedance loses its dependence on this parameter. As a result, the factor with respect to the current level, I_{rms}, can be expressed as:

$$R_{\mathrm{I}}(I_{\mathrm{rms}}) = \begin{cases} \frac{\sum_{\mathrm{i}=0}^{2} C_{\mathrm{R_I,i}} I^{i}}{\sum_{\mathrm{i}=0}^{2} C_{\mathrm{R_I,i}} I_{\mathrm{ref}}^{i}} & \hat{T}_{\mathrm{m}} < T_{\mathrm{C}} \\ 1 & \hat{T}_{\mathrm{m}} \geq T_{\mathrm{C}} \end{cases} \tag{12}$$

and

$$L_{\mathrm{I}}(I_{\mathrm{rms}}) = \begin{cases} \frac{\sum_{\mathrm{i}=0}^{2} C_{\mathrm{L_I,i}} I^{i}}{\sum_{\mathrm{i}=0}^{2} C_{\mathrm{L_I,i}} I_{\mathrm{ref}}^{i}} & \hat{T}_{\mathrm{m}} < T_{\mathrm{C}} \\ 1 & \hat{T}_{\mathrm{m}} \geq T_{\mathrm{C}} \end{cases} \tag{13}$$

As can be observed in Fig. 11a and Fig. 11b, both R and L exhibit sharp and non-monotonic variations during the steep decrease after the Curie temperature. These variations may be associated with instabilities in the model. To prevent convergence issues in the subsequent electrical simulation, this transition has been represented as a negative linear slope for the following $\Delta T = 30$ ºC above the Curie temperature T_{C}.

Table II and Table III present the coefficients to fit the temperature-dependent impedance below and above T_{C}, respectively. On the other hand, in Table IV, current-dependent coefficients are shown for temperatures below T_{C}. In consequence, the polynomial curves obtained are depicted in Fig. 11a and Fig. 11b, along with their corresponding curves obtained from Comsol Multiphysics®. As can be seen, the factorization of the equivalent resistance and inductance gives a quite accurate representation for an extended range of parameters.

TABLE II
TEMPERATURE-DEPENDENT COEFFICIENTS FOR BELOW CURIE'S POINT, $\hat{T}_{\mathrm{m}} < T_{\mathrm{C}}$

i	$C_{\mathrm{R_T,i}}$	$C_{\mathrm{L_T,i}}$
0	-0.0331	-7.6398×10^{-10}
1	5.1118×10^{-4}	5.6922×10^{-9}
2	-2.0662×10^{-6}	-2.3673×10^{-11}
3	4.6521×10^{-9}	5.4237×10^{-14}
4	-5.8262×10^{-12}	-6.8645×10^{-17}
5	3.8162×10^{-15}	4.5309×10^{-20}
6	-1.0197×10^{-18}	-1.2184×10^{-23}

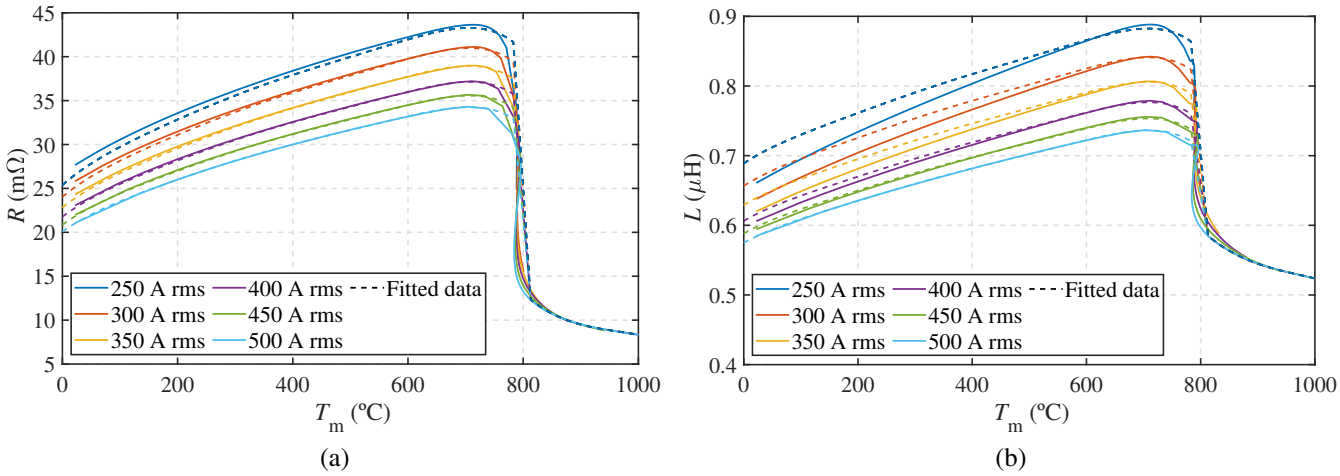

Fig. 11. Comparison of simulated data and fitted curves: (a) equivalent resistance, and (b) equivalent inductance.

TABLE III
TEMPERATURE-DEPENDENT COEFFICIENTS FOR ABOVE CURIE'S POINT, $\hat{T}_{\mathrm{m}} \geq T_{\mathrm{C}}$

i	$C'_{\mathrm{R_T,i}}$	$C'_{\mathrm{L_T,i}}$
0	1.1953	1.3487×10^{-5}
1	-0.0029	-3.0867×10^{-8}
2	2.3028×10^{-6}	2.4655×10^{-11}
3	-6.2056×10^{-10}	-6.6043×10^{-15}

TABLE IV
CURRENT-DEPENDENT COEFFICIENTS FOR BELOW CURIE'S POINT, $\hat{T}_{\mathrm{m}} < T_{\mathrm{C}}$

i	$C_{\mathrm{R_I,i}}$	$C_{\mathrm{L_I,i}}$
0	0.0585	1.1819×10^{-6}
1	-7.3044×10^{-5}	-1.4958×10^{-9}
2	4.9189×10^{-8}	1.2137×10^{-12}

V. COMPARISON OF CO-SIMULATION MODEL AND EXPERIMENTAL RESULTS

The reduced-order induction load model developed in the previous section can be used in a circuit simulation tool such as Matlab/Simulink®. This allows for obtaining the system's dynamic response under different conditions involving non-linear load behavior variations. Fig. 9 shows the model used, where the 3-phase rectifier has been replaced with a dc voltage source, $V_{\mathrm{dc},1} = 650$ V. This approach allows for simulating the last two stages to reduce computational costs without affecting the results. The objective is to simulate the complete IH process to ensure that the dynamics of the control loops remain stable even if the Curie temperature is exceeded and the load presents a substantial variation in its electrical characteristics.

For illustrative purposes, the variation of the equivalent impedance of the induction load has been represented when a cycle of 30 s duration is applied, with a current setpoint of 500 A rms. It should be noted that the model includes parasitic elements, such as the impedance of the Litz cables. These cables comprise 16000 strands, each with a diameter of 70 μm, connecting the load to the inverter output. The resistance of the wires is 7.23 mΩ, and their inductance is 2.88 μH. Additionally, the conduction resistance of the MOSFETs is $R_{\mathrm{ds}} = 1.1$ mΩ. In Fig. 12, it is observed that at around 5 seconds, the Curie temperature is reached at the center point of the load's surface, causing both components of the equivalent impedance to decrease.

Experimental validation of the results has been performed using the setup shown in Fig. 13. The abovementioned conditions were applied to obtain the results shown in Fig. 14. As depicted in Fig. 14a, the current control dynamics are fast enough to maintain a stable high current in the load during the initial transient and rapid impedance variation as the Curie temperature in the workpiece is exceeded. The simulated current follows the 500 A rms set as reference correctly with a slight ripple, which cannot be captured on the measured signal due to the bandwidth of the current sensors and sample ratio. There is observed a current overshoot at around 5 seconds, just when the middle point of the billet reaches the Curie temperature, the error on the peak is of 3.4 %; and after it the current drops slightly until it reaches an error of 2.8 % at the end of the process. These inaccuracies are within the acceptable tolerance range for this kind of industrial processes. On the other hand, in Fig. 14b, a ripple is also observed in the measured signal, which can be due to the noise effects of such small voltage values. Comparing the evolution of the dc-bus voltage with simulation results, it is concluded that it is reasonably well-regulated, considering the simplifications of the reduced model. There are two transitions clearly marked on the simulated results, related to the same transitions resulting in the equivalent resistance. This is due to the temperature-dependent expression of the equivalent resistance, divided into three ranges. As detailed in Section IV, the resistance below Curie temperature is modeled as a polynomial; then, there is a transition where a linear dependence is assumed; and for higher temperatures, its descent slope is modeled as another polynomial of lower order.

Finally, Fig. 15 shows the voltage in the resonant tank, v_{tank}, as well as the output current, i_{o}, waveforms just before to reach the Curie point and at the end of the process, verifying the proper operational conditions of the power converter.

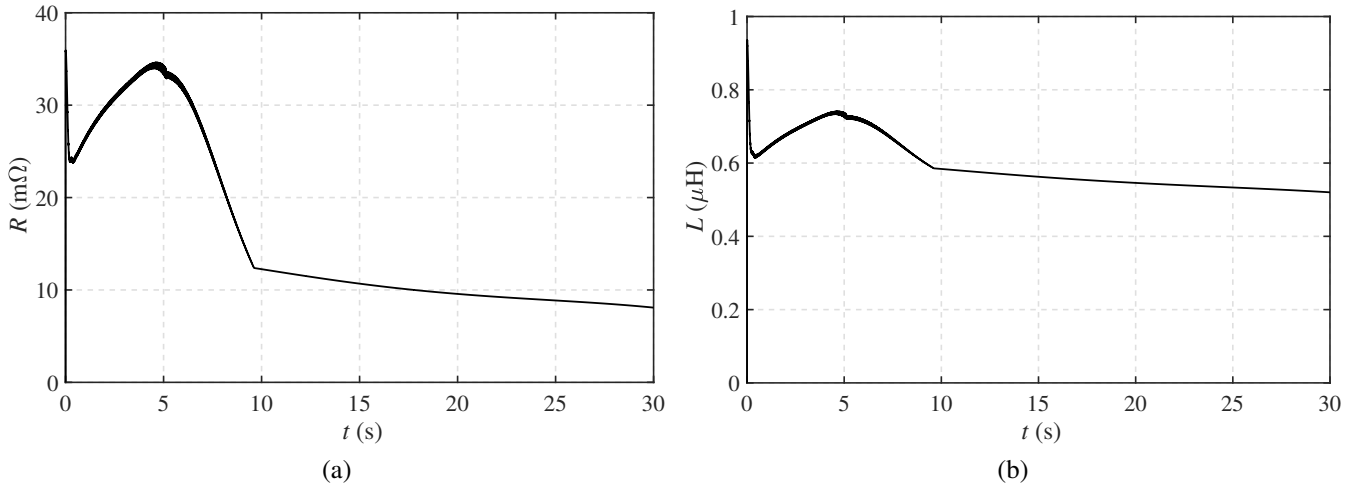

Fig. 12. Equivalent impedance for a 30 s transient in Matlab/Simulink®: (a) resistance, R, and (b) inductance, L.

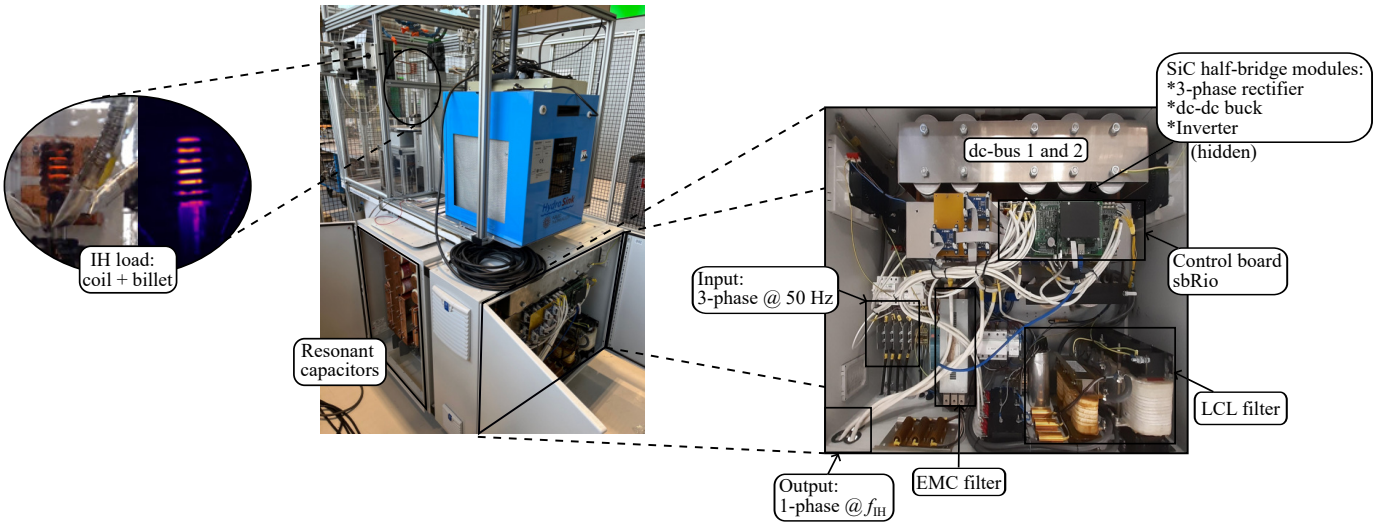

Fig. 13. Experimental setup.

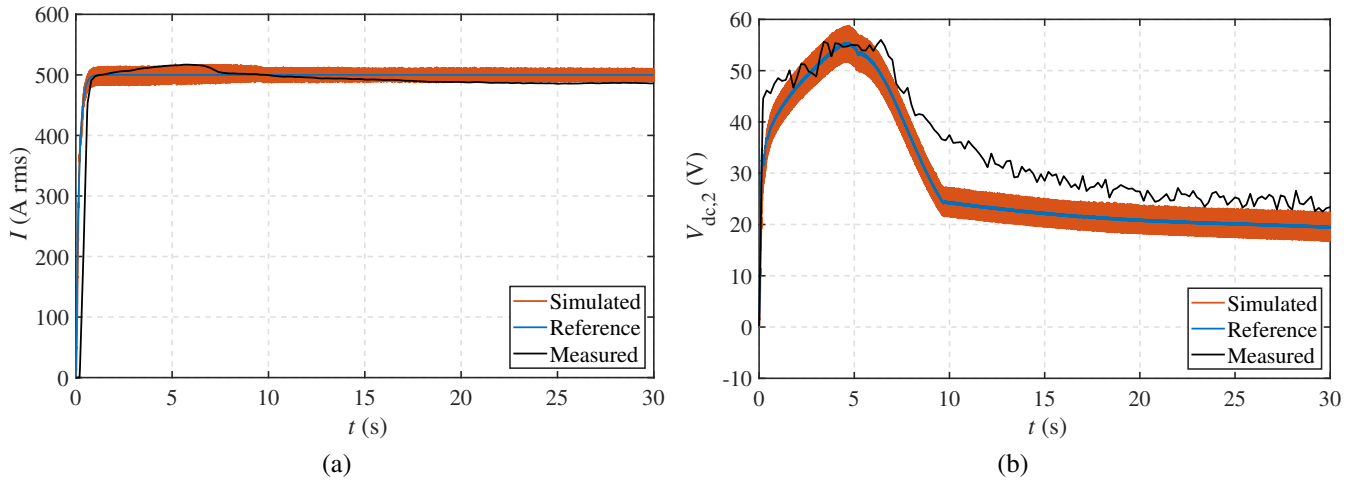

Fig. 14. Simulation results vs experimental measurements: (a) load current, and (b) regulated voltage $V_{\mathrm{dc},2}$.

VI. Conclusion

In this paper, a comprehensive description of an induction heating system for metallurgical treatments has been provided.

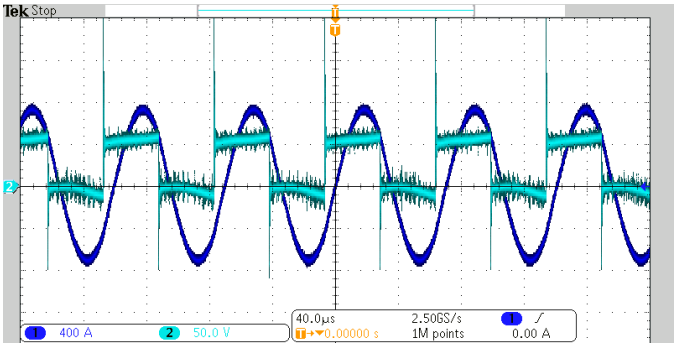

(a)

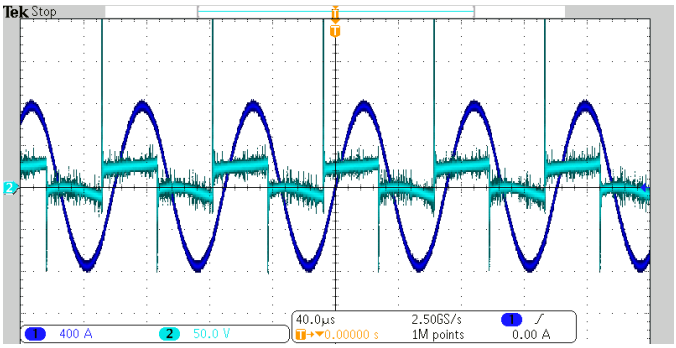

(b)

Fig. 15. Waveforms of the voltage in the resonant tank, v_{tank}, and the load current, i_{o}, at $f_{\mathrm{sw}} = 14.2$ kHz: (a) $t = 5$ s and (b) $t = 25$ s.

The associated electronics have been designed with a focus on modularity to facilitate the design process and simplicity in control to ensure robustness.

Additionally, a complete co-simulation model has been presented, which describes the physical behavior using a finite element analysis tool. The results are then used to create a reduced-order model of the load, capturing the essential characteristics of the load's nonlinear behavior. This reduced-order model is integrated into an electrical simulation tool to determine the main parameters of the electronics through computational results.

Finally, the results of the dynamic co-simulation model have been experimentally validated under real operating conditions.

REFERENCES

[1] O. Lucía, P. Maussion, E. J. Dede, and J. M. Burdío, "Induction Heating Technology and Its Applications: Past Developments, Current Technology, and Future Challenges," *IEEE Transactions on Industrial Electronics*, vol. 61, pp. 2509–2520, 2014.

[2] P. Vishnuram, G. Ramachandiran, T. S. Babu, and B. Nastasi, "Induction Heating in Domestic Cooking and Industrial Melting Applications: A Systematic Review on Modelling, Converter Topologies and Control Schemes," *Energies*, vol. 14, p. 6634, 2021.

[3] O. Lucia, J. Acero, C. Carretero, and J. Burdio, "Induction Heating Appliances: Toward More Flexible Cooking Surfaces," *IEEE Industrial Electronics Magazine*, vol. 1, no. September, pp. 35–47, 2013.

[4] J. Acero, J. M. Burdio, L. A. Barragan, D. Navarro, R. Alonso, J. R. García, F. Monterde, P. Hernandez, S. Llorrente, and I. Garde, "Domestic Induction Appliances: an Overview of Recent Research," *IEEE Industry Applications Magazine*, vol. 16, no. 2, pp. 39–47, 2010.

[5] J. W. Kolar and T. Friedli, "The Essence of Three-Phase PFC Rectifier Systems—Part I," *IEEE Transactions on Power Electronics*, vol. 28, pp. 176–198, 2013.

[6] T. Friedli, M. Hartmann, and J. W. Kolar, "The Essence of Three-Phase PFC Rectifier Systems—Part II," *IEEE Transactions on Power Electronics*, vol. 29, pp. 543–560, 2014.

[7] H. W. E. Koertzen, J. A. Ferreira, and V. Wyk, "A Comparative Study of Single Switch Induction Heating Converters Using Novel Component Effectivity Concepts," in *23rd Annual IEEE Power Electronics Specialists Conference PESC '92 Record.*, 1992.

[8] H. Sarnago, J. M. Burdio, and O. Lucia, "Dual-Output Extended-Power-Range Quasi-Resonant Inverter for Induction Heating Appliances," *IEEE Transactions on Power Electronics*, vol. 38, no. 3, pp. 3385–3397, 2023.

[9] C. Chen, Y. Chen, Y. Li, Z. Huang, T. Liu, and Y. Kang, "An SiC-Based Half-Bridge Module with an Improved Hybrid Packaging Method for High Power Density Applications," *IEEE Transactions on Industrial Electronics*, vol. 64, no. 11, pp. 8980–8991, 2017.

[10] T. Mishima, C. Takami, and M. Nakaoka, "A New Current Phasor-Controlled ZVS Twin Half-Bridge High-Frequency Resonant Inverter for Induction Heating," *IEEE Transactions on Industrial Electronics*, vol. 61, no. 5, pp. 2531–2545, 2014.

[11] N. J. Park, D. S. Lee, and D. Y. Hyun, "A Power-Control Scheme with Constant Switching Frequency in Class-D Inverter for Induction-Heating Jar Application," *IEEE Transactions on Industrial Electronics*, vol. 54, no. 3, pp. 1252–1260, 2007.

[12] F. Forest, S. Faucher, J.-Y. Gaspard, D. Montloup, J.-J. Huselstein, and C. Joubert, "Frequency-Synchronized Resonant Converters for the Supply of Multiwinding Coils in Induction Cooking Appliances," *IEEE Transactions on Industrial Electronics*, vol. 54, 2007.

[13] E. J. Dede, J. V. Gonzalez, J. A. Linares, J. Jordan, and D. Ramirez, "25-kW / 50-kHz Generator for Induction Heating," *IEEE Transactions on Industrial Electronics*, vol. 38, no. 3, pp. 203–209, 1991.

[14] A. Shenkman, B. Axelrod, and V. Chudnovsky, "Assuring Continuous Input Current Using a Smoothing Reactor in a Thyristor Frequency Converter for Induction Metal Melting and Heating Applications," *IEEE Transactions on Industrial Electronics*, vol. 48, no. 6, pp. 1290–1292, 2001.

[15] V. Esteve, J. Jordán, E. J. Dede, E. Sanchis-Kilders, P. J. Martinez, E. Maset, and D. Gilabert, "Optimal LLC Inverter Design With SiC MOSFETs and Phase Shift Control for Induction Heating Applications," *IEEE Transactions on Industrial Electronics*, vol. 69, pp. 11 100–11 111, 2022.

[16] V. Esteve, J. Jordán, E. J. Dede, P. J. Martinez, K. J. Ferrara, and J. L. Bellido, "Comparative Analysis and Improved Design of LLC Inverters for Induction Heating," *IET Power Electronics*, vol. 16, pp. 1754–1764, 8 2023.

[17] S. Komeda and H. Fujita, "A Phase-Shift-Controlled Direct AC-to-AC Converter for Induction Heaters," *IEEE Transactions on Power Electronics*, vol. 33, no. 5, pp. 4115–4124, 2018.

[18] R. C. M. Gomes, M. A. Vitorino, D. A. Acevedo-Bueno, and M. B. D. R. Correa, "Multiphase Resonant Inverter with Coupled Coils for AC-AC Induction Heating Application," *IEEE Transactions on Industry Applications*, vol. 56, no. 1, pp. 551–560, 2020.

[19] S. Inami and S. Komeda, "A Three-Phase AC Input Induction Heating System With Heat Distribution Control Capability," *IEEE Transactions on Industrial Electronics*, vol. PP, pp. 1–11, 2024.

[20] R. C. M. Gomes, M. A. Vitorino, D. A. Acevedo-Bueno, and M. B. D. R. Correa, "Three-Phase AC-AC Converter with Diode Rectifier for Induction Heating Application with Improved Input Current Quality and Coil Modeling," *IEEE Transactions on Industry Applications*, vol. 57, no. 3, pp. 2673–2681, 2021.

[21] P. Guillen, H. Sarnago, O. Lucia, and J. M. Burdio, "GaN-Based Matrix Resonant Power Converter for Domestic Induction Heating," *IEEE Transactions on Power Electronics*, vol. 38, no. 6, pp. 6769–6773, 2023.

[22] J. M. Espí Huerta, E. J. Dede García Santamaría, R. García Gil, and J. Castelló-Moreno, "Design of the L-LC Resonant Inverter for Induction Heating Based on its Equivalent SRI," *IEEE Transactions on Industrial Electronics*, vol. 54, no. 6, pp. 3178–3187, 2007.

[23] L. A. Barragán, D. Navarro, J. Acero, I. Urriza, and J. M. Burdio, "FPGA Implementation of a Switching Frequency Modulation Circuit for EMI Reduction in Resonant Inverters for Induction Heating Appliances," *IEEE Transactions on Industrial Electronics*, vol. 55, no. 1, pp. 11–20, 2008.

[24] J. Zerad, S. Riachy, P. Toussaint, and J. P. Barbot, "Novel Phasor Transformation for Feedback Control Design of Induction Heating Systems with Experimental Results," *IEEE Transactions on Industrial Electronics*, vol. 62, pp. 6478–6485, 10 2015.

[25] H. Fujita and H. Akagi, "Pulse-Density-Modulated Power Control of a 4 kW, 450 kHz Voltage-Source Inverter for Induction Melting Applica-

tions," *IEEE Transactions on Industry Applications*, vol. 32, no. 2, pp. 279–286, 1996.

[26] V. Esteve, E. Sanchis-Kilders, J. Jordán, E. J. Dede, C. Cases, E. Maset, J. B. Ejea, and A. Ferreres, "Improving the Efficiency of IGBT Series-Resonant Inverters Using Pulse Density Modulation," *IEEE Transactions on Industrial Electronics*, vol. 58, no. 3, pp. 979–987, 2011.

[27] J. Egalon, S. Caux, P. Maussion, M. Souley, and O. Pateau, "Multiphase System for Metal Disc Induction Heating: Modeling and RMS Current Control," *IEEE Transactions on Industry Applications*, vol. 48, pp. 1692–1699, 2012.

[28] X. Zhe and P. Sanqiang, "Temperature Optimal Control of the Casting Billet Induction Heating Process Based on the BP Prediction Model," *Proceedings of the 2013 IEEE Symposium on Computational Intelligence in Control and Automation, CICA 2013 - 2013 IEEE Symposium Series on Computational Intelligence, SSCI 2013*, pp. 163–167, 2013.

[29] B. Meziane and H. Zeroug, "Comprehensive Power Control Performance Investigations of Resonant Inverter for Induction Metal Surface Hardening," *IEEE Transactions on Industrial Electronics*, vol. 63, pp. 6086–6096, 10 2016.

[30] A. Bitoleanu, M. Popescu, and V. Suru, "Shift Phase Power Control in Induction Heating Systems with Voltage Resonant Inverter," *2014 International Conference on Applied and Theoretical Electricity, ICATE 2014 - Proceedings*, 12 2014.

[31] I. Yilmaz, E. Durna, and M. Ermis, "Design and Implementation of a Hybrid System for the Mitigation of PQ Problems of Medium-Frequency Induction Steel-Melting Furnaces," *IEEE Transactions on Industry Applications*, vol. 52, no. 3, pp. 2700–2713, 2016.

[32] M. Fisk, M. Ristinmaa, A. Hultkrantz, and L. E. Lindgren, "Coupled Electromagnetic-Thermal Solution Strategy for Induction Heating of Ferromagnetic Materials," *Applied Mathematical Modelling*, vol. 111, pp. 818–835, 2022.

[33] J. Barglik, "Mathematical Modeling of Induction Surface Hardening," *COMPEL: The International Journal for Computation and Mathematics in Electrical and Electronic Engineering*, vol. 35, pp. 1403–1417, 1 2016.

[34] M. Spezzapria, M. Forzan, and F. Dughiero, "Numerical Simulation of Solid-Solid Phase Transformations during Induction Hardening Process," *IEEE Transactions on Magnetics*, vol. 52, no. 3, pp. 1–4, 2016.

[35] M. Areitioaurtena, U. Segurajauregi, V. Akujärvi, M. Fisk, I. Urresti, and E. Ukar, "A Semi-Analytical Coupled Simulation Approach for Induction Heating," *Advanced Modeling and Simulation in Engineering Sciences*, vol. 8, 2021.

[36] I. Yilmaz, Ö. Salor, M. Ermiş, and I. Çadirci, "Field-Data-Based Modeling of Medium-Frequency Induction Melting Furnaces for Power Quality Studies," *IEEE Transactions on Industry Applications*, vol. 48, no. 4, pp. 1215–1224, 2012.

[37] K. L. Nguyen, O. Pateau, S. Caux, P. Maussion, and J. Egalon, "Robustness of a Resonant Controller for a Multiphase Induction Heating System," *IEEE Transactions on Industry Applications*, vol. 51, pp. 73–81, 1 2015.

[38] D. M. Choudhary and C. D. Kotwal, "Analysis of Load Dynamics in Induction Melting Furnace and Improved Power Quality with Phase Shift Modulated LLC Resonant IGBT Inverter," *IEEE Journal of Emerging and Selected Topics in Power Electronics*, vol. 11, no. 5, pp. 4681–4692, 2023.

[39] G. Huang, F. Ma, H. Ding, Q. Yang, R. Fan, and L. Wang, "Dual Fundamental Frequency HSS-Based Reduced Order Impedance Modeling of AC/AC Modular Multilevel Converter for Tundish Heating," *IEEE Transactions on Power Delivery*, vol. 39, no. 3, pp. 1749–1760, 2024.

[40] A. Mendi-Altube, I. Villar, C. Carretero, and J. Acero, "Dynamic DC-Bus Voltage Control of Induction Hardening System Under Load Temperatures from Ambient to Beyond Curie Point," in *2024 IEEE Applied Power Electronics Conference and Exposition (APEC)*. IEEE, 2 2024, pp. 1669–1674.

[41] M. Fisk, L. E. Lindgren, W. Datchary, and V. Deshmukh, "Modelling of Induction Hardening in Low Alloy Steels," *Finite Elements in Analysis and Design*, vol. 144, pp. 61–75, 2018.

[42] F. Bay, V. Labbe, Y. Favennec, and J. L. Chenot, "A numerical model for induction heating processes coupling electromagnetism and thermomechanics," *International Journal for Numerical Methods in Engineering*, vol. 58, pp. 839–867, 2003.

[43] S. Yin, L. D. Rienzo, X. Ma, and Y. Huangfu, "Boundary element formulation enforcing high-order surface impedance boundary conditions for axisymmetric eddy current problems," *IEEE Transactions on Magnetics*, vol. 57, pp. 1–9, 2021.

[44] C. Carretero, J. Acero, and J. M. Burdio, "Normalized Nonlinear Impedance Boundary Condition in Anhysteretic Magnetic Material for Eddy Current Problems," *IEEE Transactions on Magnetics*, 2024.

[45] O. Lahuerta, J. Ortega, C. Carretero, J. P. Martinez, and J. Acero, "Fröhlich model characterization of magnetic properties of the induction heating load," *COMPEL - The international journal for computation and mathematics in electrical and electronic engineering*, vol. ahead-of-print, 2024. [Online]. Available: https://doi.org/10.1108/COMPEL-09-2023-0427

[46] A. Mendi-Altube, I. Villar, C. Carretero, and J. Acero, "Electro-Thermal Modeling of an Induction Heating Process of 42CrMo4 Steel Probe," *International Journal of Applied Electromagnetics and Mechanics*, vol. 75, pp. 169–178, 2024.

[47] D. Coupard, T. Palin-luc, P. Bristiel, V. Ji, and C. Dumas, "Residual Stresses in Surface Induction Hardening of Steels: Comparison Between Experiment and Simulation," *Materials Science and Engineering A*, vol. 487, pp. 328–339, 7 2008.

Amaiur Mendi-Altube received the B.Sc. degree in Renewable Energies Engineering from the University of the Basque Country (UPV/EHU), Spain, in 2019, and the M.Sc. degree in Energy and Power Electronics from Mondragon Unibertsitatea (MU), Spain, in 2021. Since 2019, she has been a Researcher with the Ikerlan Technology Research Centre, Arrasate-Mondragón, where nowadays she is pursuing her Ph.D. in collaboration with the University of Zaragoza. Her current research interests include the design and optimization of power converters for electromagnetic induction heating technologies, and electro-thermal finite elements modeling of the processes.

Irma Villar (Member, IEEE) received the B.Sc. and M.Sc. degrees in electronics from Mondragon Unibertsitatea (MU), Mondragón, Spain, in 2003 and 2005, respectively, and the Ph.D. degree in power electronics from the Federal Institute of Technology Lausanne (EPFL), Switzerland, in 2010.Since 2009, she has been a Researcher and Project Manager in power electronics with the IKERLAN Technology Research Center, Basque Research and Technology Alliance (BRTA), Mondragón, in several industrial and research projects related to power conversion systems for railway traction, electric vehicle, household applications, and aeronautics. Since 2016, she has also been Electromagnetism and Converters Control Team Leader. Her fields of experience are the design of electromagnetic devices, such as transformers, inductors, and inductive transfer and heating systems.

Claudio Carretero (Senior Member, IEEE) received the M.Sc. degree in physics and the M.Eng. and Ph.D. degrees in electrical engineering from the University of Zaragoza, Zaragoza, Spain, in 1998, 2002, and 2010, respectively. He is currently an Associate Professor with the Department of Applied Physics, University of Zaragoza. His research interests include induction heating applications and electromagnetic modeling of inductive systems. Dr. Carretero is a member of the Instituto de Investigacion en Ingenieria de Aragon (I3A).

Jesús Acero (Senior Member, IEEE) received the M.Sc. and Ph.D. degrees in electrical engineering from the University of Zaragoza, Zaragoza, Spain, in 1992 and 2005, respectively. From 1992 to 2000, he worked on several industry projects, especially focused on custom power supplies for research laboratories. Since 2000 he has been with the Department of Electronic Engineering and Communications at the University of Zaragoza, Spain, where he is currently a Professor. His main research interests include resonant converters for induction heating applications, inductive-type load modeling, and electromagnetic modeling. Dr. Acero is a Member of the IEEE Power Electronics, Industrial Electronics, and Magnetics Societies. Dr. Acero is a member of the Instituto de Investigación en Ingeniería de Aragón (I3A).